Direct S_N2 or S_N2X Manifold – Mechanistic Study of Ion-Pair Catalyzed Carbon(sp^3)-Carbon(sp^3) Bond Formation

Richmond Lee,[1,2*] Chi Bong Eric Chao,[1,2] Xu Ban,[3] Siu Min Tan,[4] Haibo Yu,[1,2] Christopher J. T. Hyland,[1,2] and Choon-Hong Tan[3]

[1] School of Chemistry and Molecular Bioscience, University of Wollongong, Northfields Avenue, Wollongong, NSW 2522, Australia

[2] Molecular Horizons, University of Wollongong, Northfields Avenue, Wollongong, NSW 2522, Australia

[3] Division of Chemistry and Biological Chemistry, Nanyang Technological University, 21 Nanyang Link, Singapore 637371

[4] Singapore University of Technology and Design, 8 Somapah Rd, Singapore 487372

ABSTRACT: Density functional theory (DFT) is used in this work to predict the mechanism for constructing congested quaternary-quaternary carbon(sp^3)–carbon(sp^3) bonds in a pentanidium catalyzed substitution reaction. Computational mechanistic studies were carried out to investigate the proposed S_N2X manifold, which consists of two primary elementary steps: halogen atom transfer (XAT) and subsequent S_N2. For the first calculated model on original experimental substrates, XAT reaction barriers were more kinetically competitive than an S_N2 pathway and connects to thermodynamically stable intermediates. Extensive computational screening-modelling were then done on various substrate combinations designed to study steric influence and to understand the mechanistic rationale, and calculations reveal that sterically congested substrates prefer the S_N2X manifold over S_N2. Different halides as leaving groups were also screened and it was found that the reactivity increases in order of Br > Cl > F in agreement of the strength of C–X bonds. However, DFT modelling suggests that chlorides can be a viable substrate for the S_N2X process which should be further explored experimentally. Finally, ONIOM calculations on the full catalyst model were carried out to rationalize the stereoselectivity which corroborates with experimental results.

■ INTRODUCTION

Substitution reactions are of fundamental importance to chemical synthesis and also occur in important biological processes. The common variants of substitution mechanism are bimolecular nucleophilic substitution (S_N2), unimolecular nucleophilic substitution (S_N1), internal nucleophilic substitution (S_Ni) or as a continuum between S_N1 and S_N2,[1,2] and in depth basic understanding of substitution mechanism can reveal important insights into a reaction (Figure 1A).[3,4] In contrast to the well-established backside attack observed for S_N2 reactions, another possible S_N2 substitution mechanism involves frontside nucleophilic attack on the leaving group - a possibility not considered here due to steric hindrance.[7] Halogenophilic substitution (S_N2X) on the other hand is less known process, and the mechanistic details of these processes are only just starting to be understood.[5,6] These distinct mechanistic differences between substitution reactions are depicted in Figure 1, whereby to distinguish these mechanistic variances solely by experimental data is not always possible. Therefore, computational mechanistic studies of substitution mechanisms have been pivotal to enrich the understanding of these processes in both chemical and biological systems.[8]

An S_N2X process in chiral cationic pentanidium-catalyzed carbon-sulfur bond formation have been previously uncovered by our groups using DFT and experimental techniques. [9] Recent progress on this topic predicted an S_N2X pathway occurring in the base-mediated isomerization of halide substrate in relation to forming chiral carbon-nitrogen bond through a proposed dynamic kinetic resolution model (Figure 1B).[10] These studies highlighted an important facet of substitution reactions operating *via* the less commonly explored S_N2X pathway towards forging highly desirable, but synthetically challenging carbon-heteroatom bonds. In these examples, both DFT and experimental studies played a synergistic and instrumental role in clarifying the reaction mechanism and chemical characteristics of S_N2X and enabled elegant reaction design strategies to achieve a library of difficult-to-make compounds.

Very recently, the experimental investigation of the halogenophilic substitution reaction catalyzed by pentanidium was further extended to highly challenging quaternary-tertiary or quaternary-quaternary carbon(sp^3)-carbon(sp^3) bond formation.[11,12] The halogenophilic substitution or S_N2X manifold proposed for this process is enantio-convergent, which leads to an interesting departure to the putative S_N1 or $S_{RN}1$ mechanism that is usually expected to operate for such sterically hindered substrates. In

the context of this work, the S_N2X manifold consists of two primary elementary steps which are halogen atom transfer (XAT) and S_N2. To fully understand the chemistry behind this intriguing substitution reaction involving vicinal quaternary carbon(sp^3)-carbon(sp^3) bond formation, quantum chemical calculations were performed to predict and rationalize the S_N2 and S_N2X dichotomy (Figure 1C). To take a step further, DFT modelling was carried out to predict if chlorides and fluoride which have stronger C-X bonds and are expected to be more challenging to activate could undergo the S_N2X manifold. Finally computational modelling of the full chiral catalyst model was carried out to rationalize the stereochemistry of this enantiospecific process.

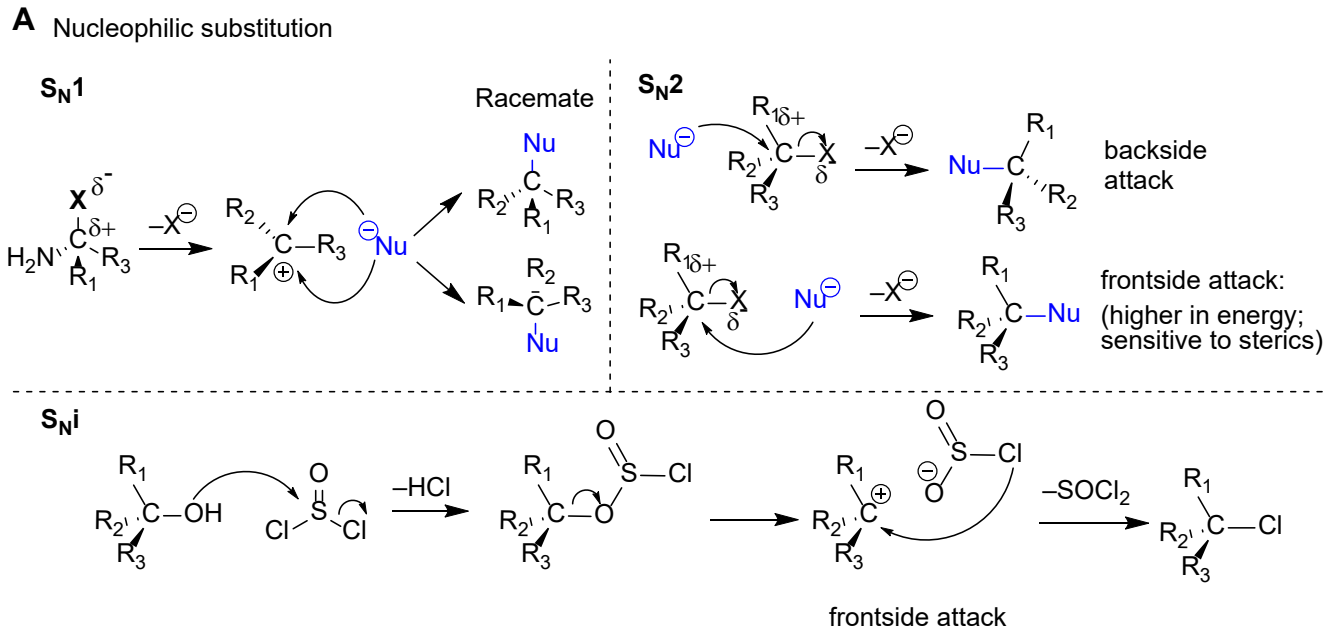

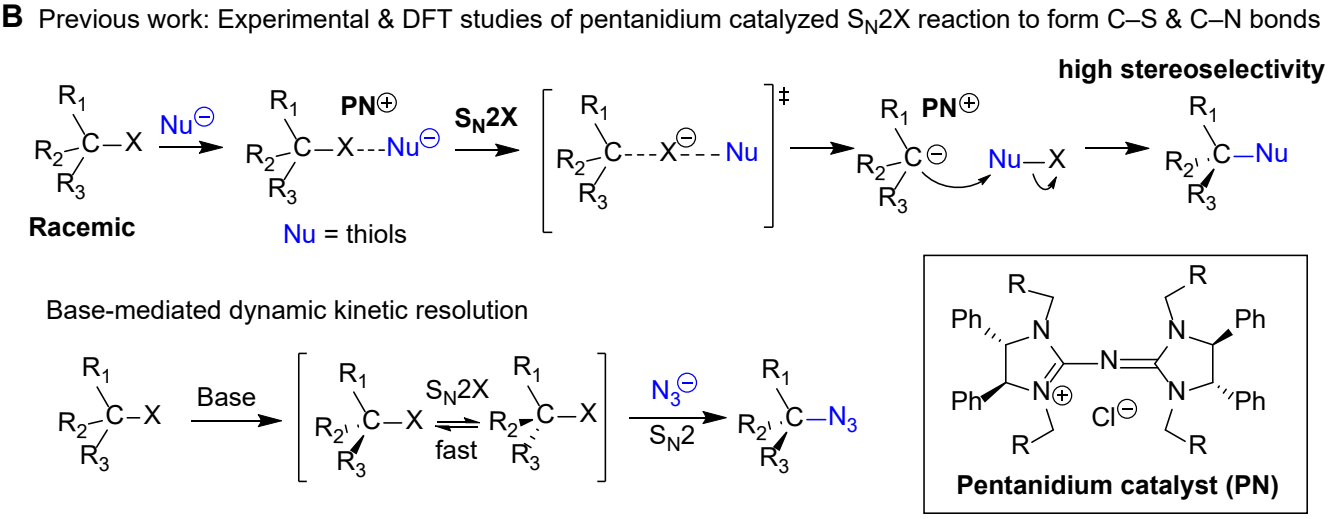

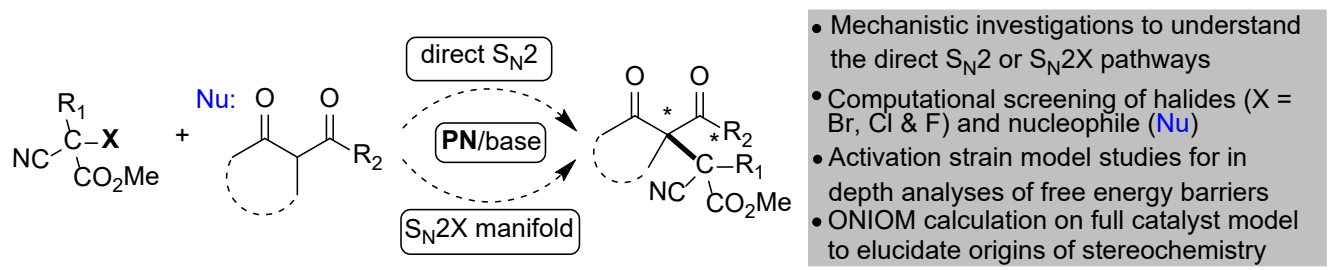

Figure 1 - A) Comparison of nucleophilic substitution variances, B) previous work on S_N2X chemistry and C) objectives of this work

■ COMPUTATIONAL METHODS

Conformational search and DFT calculations. Grimme's CREST iMTD-GC algorithm,[13] combined with the extended semi-empirical tight binding method GFN2-xTB,[14] was used to provide initial structural predictions of most stable conformers. Conformations of ion pair complexes were optimized with the implicit solvent GFN2(ALPB) model with toluene parameter in "NCI" mode. The most stable energy conformers were then further optimized with DFT, carried out with Gaussian 16 computational chemistry suite.[15] Gas phase geometry optimization of minimum and transition state electronic structures were performed at this level of theory: Minnesota functional M11,[16] and Pople's basis set 6-31G(d,p),[17] and Stuttgart-Dresden effective core potential (SDD) for Cs atom.[18,19] Frequency calculations were carried out at that level to ensure convergence - positive eigenvalues for minima and one single negative for saddle points - corrected with the quasiharmonic approximated frequencies,[20] where frequencies < 100 cm^{-1} were scaled to 100 cm^{-1}. Thermochemical corrections and zero point vibrational energies were thus determined at the gas phase M11 functional level and corrected. Solvation energies were considered with single point calculations with the SMD model,[21] with toluene parameters on the gas phase optimized structures at this level of theory: M11/def2-TZVP[22,23]. The M11/def2-TZVP energies together with thermal and vibrational corrections based on gas-phase vibrations constitute the relative solution free energy, ΔG_{sol}, reported herein. The ΔG_{sol} is corrected to consider passage of 1 atm gas into 1M in solution, $\Delta G^{1atm \rightarrow 1M}$ as follows:

$\Delta G^{1atm \rightarrow 1M} = \Delta N^* RT\ln(RT/P)$, where ΔN is the number of moles of gas change from reactant to product and $RT\ln(RT/P)$ equals to 1.89 kcal/mol at 298 K.[24]

The distortion/interaction activation strain model was further used to understand and rationalize the reactivity of the S_N2X-S_N2 pathways with the gas-phase TS structures and molecular fragments calculated at M11/def2-TZVP level of theory.[25–30]

ONIOM calculations for full catalyst model. Gas phase minimum or transition state electronic structure optimizations with the full catalyst model were carried out with ONIOM,[31] a two-layer integrated molecular orbital and molecular mechanics formalism. The molecular orbital calculation utilizes M11/6-31G(d,p) covering the catalyst core and substrates while molecular mechanics utilizes semi-empirical PM6,[32] covering the large aryl substituents of the catalyst, Gaussian keyword: oniom(m11/6-31G(d,p):pm6). Frequency calculations were also done at ONIOM(M11/6-31G(d,p):PM6) level of theory on the optimized structures. The electronic energies were improved with a higher level single-point calculation at M11/def2-TZVP. The M11/def2-TZVP energies together with thermal and vibrational corrections based on gas phase vibrations constitute the relative free energy, ΔG, reported here.

■ RESULTS AND DISCUSSION

Truncated pentanidium and first model. DFT calculations were performed to rationalize the mechanism of the quaternary C-C bond process with a truncated achiral pentadinium catalyst model (see Figure 2). Initial calculations involved modelling the molecular binding of bromide **BR1** to the catalyst-enolate complex **INT1**, which resulted in the formation of pre-S_N2 complex **INT2**, ΔG_{sol} = 1.6 kcal/mol with respect to **INT1** and **BR1**. The intermediate **INT2** is primed for direct substitution *via* the S_N2 pathway through transition state **TS1**, with a relative Gibbs free energy barrier of $\Delta G^{\ddagger}_{sol}$ = 24.4 kcal/mol with respect to **INT1** and **BR1**, generating the product **PDT** and the catalyst-bromide complex **INT3**. Another envisioned pathway proceeds *via* the halogenophilic S_N2X manifold, starting with the pre-transition intermediate **INT4** formed by coordination between intermediate **INT1** and **BR1** (ΔG_{sol} = 3.3 kcal/mol), and is held together by halogen bonding between Br and the ketoester anion,[5,33,34] the key interaction which predisposes the complex to undergo the halogen atom transfer (XAT) process. Subsequently, the halogen bonded complex **INT4** undergoes bromine atom transfer from the ketoester *via* **TS2** (with low energy barrier of $\Delta G^{\ddagger}_{sol}$ = 11.5 kcal/mol) to form a cyanoester bromide complex intermediate **INT5** (ΔG_{sol} = 4.1 kcal/mol).

The dissociation of the cyanoester bromide **BR2** from the catalyst complex **INT6** is thermodynamically stable and exergonic (ΔG_{sol} = -5.5 kcal/mol), and presents the opportunity for the ketoester bromide **BR2** to undergo isomerization with the catalyst-$CsCO_3^-$ complex **INT10**. The calculations revealed that the activation barrier for the bromine atom transfer to CO_3^{2-} is energetically feasible through **TS5**, $\Delta G^{\ddagger}_{sol}$ = 6.3 kcal/mol with respect to **INT10** and **BR2**, forming a slightly endergonic intermediate **INT12** (ΔG_{sol} = 1.7 kcal/mol).

Binding of organo-bromide **BR2** and intermediate **INT6** with the C-Br bond facing away from the carbanion generates two possible intermediates **INT7** and **INT8**, leading to two diastereomers. **INT8** undergoes S_N2 displacement *via* transition state **TS4** (overall activation barrier of $\Delta G^{\ddagger}_{sol}$ = 28.8 kcal/mol with respect to **INT6** and **BR2**) to generate the diastereomer **PDT2** and pentanidium-Br salt **INT3** (ΔG_{sol} = -27.1 kcal/mol). The predicted major diastereomer **PDT** is generated from intermediate **INT7** through a more stable transition state **TS3**, with overall solution free energy activation barrier of $\Delta G^{\ddagger}_{sol}$ = 24.9 kcal/mol with respect to **INT6** and **BR2**. In summary, using the truncated catalyst model, DFT calculations predict a more energetically accessible pathway *via* the S_N2X instead of the direct S_N2 displacement, due to a more energetically competitive XAT process and the preferential thermodynamic stability of the **INT6** and **BR2** intermediates. At this point, the isomerization of the

ketoester bromide **BR2** to occur, which allows for dynamic kinetic resolution in the chiral catalyst version, as suggested by previous DFT studies.[9,10]

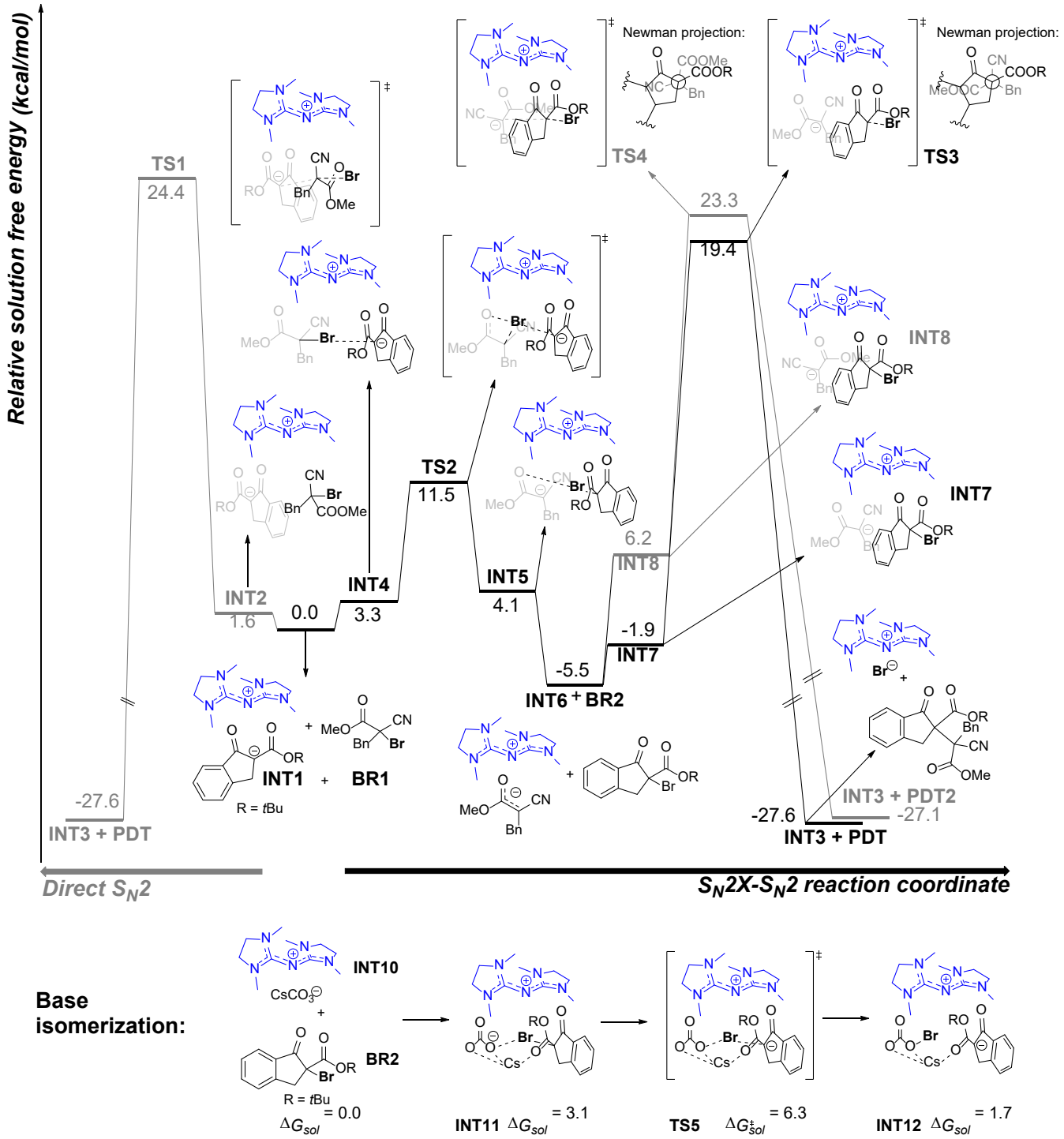

Figure 2 - Relative solution free energy profile delineating the one-step S_N2 and S_N2X-S_N2 pathways (top) and base isomerization of BR2 (bottom). DFT calculations at M11/def2-TZVP/SMD(toluene)//M11/BS1 level of theory. BS1: ECP basis set SDD was used for Cs atom while all electron 6-31(d,p) for the rest of atoms. Energy values are in kcal/mol.

Computational screening of electrophiles/nucleophiles. Computational screening of various electrophiles and nucleophiles were carried out to predict reactivity and to further investigate the structure-electronic relation in the truncated pentanidium model. The first part involved replacing the cyclic ketoester nucleophile with the malonate ester (**1-1**), whereby the free energy barrier for S_N2 pathway *via* **TS1_1-1** (see Table 1, $\Delta G^{\ddagger}_{sol}$ = 24.8 kcal/mol) was calculated to be nearly isoenergetic to the cyclic ketoester. For the S_N2X manifold, the first XAT step *via* **TS2_1-1** (see Table 1, $\Delta G^{\ddagger}_{sol}$ = 11.8 kcal/mol) is nearly isoenergetic to **TS2** but forms a very stable intermediate pair **INT6_1-1** and malonate ester bromide **BR2_1-1** (-9.5 kcal/mol relative to the

starting species). The overall barrier for the concomitant S_N2 step **TS3_1-1**, $\Delta G^{\ddagger}_{sol}$ = 23.3 kcal/mol taken with reference to **INT6_1-1** and **BR2_1-1**, is slightly lower than that of the cyclic ketoester's second S_N2 free energy barrier of 24.9 kcal/mol. This difference can be rationalized by a less rigid nucleophile and as demonstrated by the comparison of the entropy component for $\Delta S^{\ddagger}_{sol}$ (**TS3_1-1** is -26.5 versus **TS3** -43.2 cal/mol-K at 298 K).

Table 1 - Computational screening of bromo-, chloro-, and fluoro-cyanoesters and malonate esters. DFT calculations at M11/def2-TZVP/SMD(toluene)//M11/6-31G(d,p) level of theory. Values are solution free energies in kcal/mol relative to respective **INT1** + **X1**.

1-1 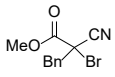 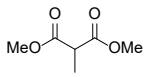

1-2 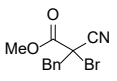 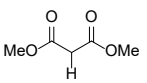

2-1 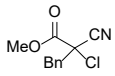 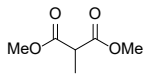

3-1 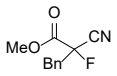 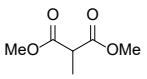

4-1 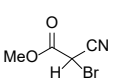 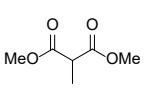

4-2 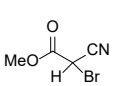 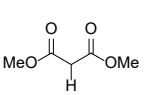

Substrate set (#):	1-1	1-2	2-1	3-1	4-1	4-2
TS1_#	24.8	26.2	28.6	38.4	17.6	18.6
INT4_#	7.9	9.2	4.7	9.6	10.0	10.1
TS2_#	11.8	13.7	20.0	55.1	10.8*	12.1
INT6_# + X2_#	-9.5	-4.8	-10.0	-10.0	-12.9	-8.2
TS3_#	13.8	15.0	17.7	28.6	11.3	11.8

*Optimized to a minimum structure

Substituting the methyl group on the α-carbon of the malonate ester with hydrogen could effectively aid in mitigating the reaction barrier due to lowered steric repulsion between the substrates. The **1-2** substrate set (Table 1) was modelled and calculations revealed that the direct S_N2 pathway barrier, **TS1_1-2**, at $\Delta G^{\ddagger}_{sol}$ = 26.2 kcal/mol is significantly higher than that of **TS1_1-1**. The XAT barrier through **TS2_1-1** is also higher at 13.7 kcal/mol and the intermediate pair **INT6_1-1** and **BR2_1-2** were calculated to be energetically less stable than **1-1** at -4.8 kcal/mol. The overall barrier for the S_N2 elementary step in the S_N2X manifold through **TS3_1-2** was calculated to be much more accessible at 19.8 kcal/mol due to the cyanoester carbanion attacking a less hindered sp^3 carbon. Further replacing the benzyl group with H on the cyanoester (**4-1** and **4-2**) lowered the **TS1** barrier significantly to about 18 kcal/mol on average. The **TS2** XAT barrier for **4-2** and estimated barrier for **4-1**, (no TS with imaginary frequency could be optimized for this structure), are 12.1 and 10.8 kcal/mol respectively – which are close to **TS2_1-1** and **TS2_1-2**. The **TS3** barriers relative to **INT6** and **BR2** intermediate pair are higher: 24.2 and 20.0 kcal/mol for **4-1** and **4-2**. This suggests that the less sterically bulky cyanoester bromide electrophile could steer the reaction pathway towards direct S_N2 for making quaternary-tertiary (**4-1**) and tertiary-tertiary (**4-2**) C-C bonds in the first instance. The corollary of a direct S_N2 is the negative impact on stereo-convergence as the formation of the resting state **INT6** + **BR2** that is important for dynamic kinetic resolution *via* isomerization of **BR2** through **TS5** is restricted.

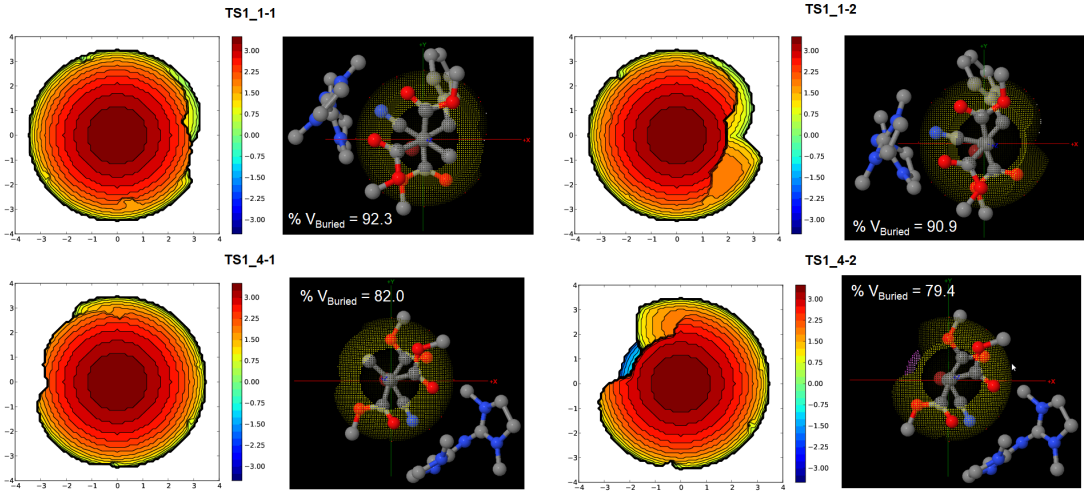

Figure 3 – Buried volume plots of TS1 structures of 1-1, 1-2, 4-1 and 4-1. Isocontour steric map in Å – red for hindered and blue for less hindered regions. % V_{Buried} is the percentage buried volume based and centered on the cyanoester. Left of steric map are the corresponding molecular perspectives.

The SambVca code was used to qualitatively visualize the steric environment of the S_N2 **TS1** transition state structures of **1-1**, **1-2**, **4-1** and **4-2** centered on the cyanoester (see Figure 3).[35] The buried volume plot shows that the more sterically congested substrates **1-1** and **1-2** have higher % of buried volume (91 to 92) directly translates to higher **TS1** activation barrier energies (~25 kcal/mol), compared to **4-1** and **4-2** (79 to 82%) which have lower **TS1** barrier (~18 kcal/mol).

Next, the scope of the electrophiles was extended to include cyanoester chloride (**2-1**) and fluoride (**3-1**) (see Table 1), both have stronger C-X bond than C-Br and might lead to higher free energy barriers for the S_N2 or S_N2X processes. As expected, the calculated barriers for direct S_N2 through **TS1_2-1** is higher at 28.6 kcal/mol (compared with **TS1_1-1** at 24.8 kcal/mol), and even much higher for **TS1_3-1** at 38.4 kcal/mol. The free energy barriers for the XAT process for **2-1** and **3-1** also increased in comparison to **1-1**: **TS2_2-1** at 20.0 kcal/mol which is kinetically accessible but **TS2_3-1** is prohibitively high at 55.1 kcal/mol. The rate determining second S_N2 displacement process of the S_N2X manifold, through **TS3_2-1** and **TS3_3-1** were determined to be 27.7 and 38.6 kcal/mol respectively. Computational modelling suggests that it is energetically feasible for chloride to undergo S_N2X but highly unlikely for fluoride.

Computational screening of chlorides. To computationally predict if chlorides can undergo the S_N2X manifold with reasonable energies, attention was next turned towards computational screening of cyanoester chloride with various malonate ester nucleophiles. Beginning with **2-2**, the calculated **TS1_2-2** and **TS2_2-2** $\Delta G^{\ddagger}_{sol}$ at 30.1 and 21.8 kcal/mol (see Table 2 entry **2-2**), relative to **INT1_2-2** and **Cl1_2-2** respectively, are slightly higher than **2-1**. As the **INT6_2-2** and **Cl2_2-2** energies become less exergonic or less stable, the activation barrier for **TS3_2-2** with $\Delta G^{\ddagger}_{sol}$ = 25.0 kcal/mol relative to **INT6_2-2** and **Cl2_2-2** decreases. Substituting the hydrogen with electronegative fluorine (**2-3**) results in stabilized **TS1_2-3**, **TS2_2-3** and **TS3_2-3** energies at 27.5, 19.2 and 17.1 kcal/mol relative to **INT1_2-3** and **Cl1_2-3** respectively; the overall barrier for **TS3_2-3** improved to 24.3 kcal/mol with respect to **INT6_2-3** and **Cl2_2-3**. However, the presence of highly electron-withdrawing but bulky -CF_3 group (**2-4**) raises the barriers significantly to 38.1, 27.6 and 43.2 kcal/mol for **TS1_2-4**, **TS2_2-4** and **TS3_2-4**. Having phenyl substituents on the malonate ester gave higher calculated barriers compared to others (see Table 2 entries **2-5**, **2-6** and **2-7**). Computational modelling revealed that the presence of electron-withdrawing group (-NO_2) on the phenyl *para* position (**2-6**) raises the barrier for XAT, **TS2_2-6** with 29.3 kcal/mol due to a less reactive anion towards abstracting the Cl, whereas species containing electron-donating -OMe (**2-7**) moiety enhances nucleophilicity and lowers barrier for XAT.

Table 2 - Computational screening of chloro-cyanoesters and various malonate esters. DFT calculations at M11/def2-TZVP/SMD(toluene)//M11/6-31G(d,p) level of theory. Values are solution free energies in kcal/mol relative to **INT1** + **Cl1**.

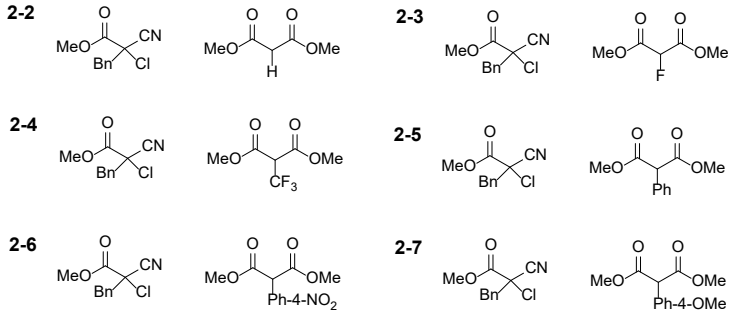

Substrate set (#):	2-2	2-3	2-4	2-5	2-6	2-7
TS1_#	30.1	27.5	38.1	33.9	36.8	33.0
TS2_#	21.8	19.2	27.6	27.0	29.3	26.2
INT6_# + Cl2_#	-4.9	-7.2	4.7	-4.2	1.6	-5.6
TS3_#	19.1	17.1	43.2	27.7	32.0	25.8

Distortion/interaction activation strain model analyses. To further dissect the energies qualitatively and examine the mechanistic preference of the examples *vide supra*, as well as rationalize the competition between diastereomeric **TS3** and **TS4**, distortion/interaction activation strain modelling was carried out (see Figure 4).[26] The activation strain model revealed higher strain energy, $\Delta E^{\ddagger}_{strain}$, for **TS1** (50.8 kcal/mol) as a result of unfavorable geometry distortion in the transition state, followed by **TS3** (43.9 kcal/mol) and **TS4** (49.5 kcal/mol). The activation energy $\Delta E^{\ddagger}_{activation}$ follow a similar trend with **TS3** having the smaller $\Delta E^{\ddagger}_{activation}$ than **TS1** or **TS4**. These energies suggest that through **TS1** or the direct S_N2 process, the nucleophilic approach by the ketoester carbanion towards the cyanoester bromide is not ideal, which results in the strain energy $\Delta E^{\ddagger}_{strain}$ for **TS1** to be much higher than **TS3** or **TS4**. Diastereo-selection could be controlled by the second displacement step of the S_N2X manifold through **TS3** and **TS4**. The more stable transition state **TS3** has a significantly lower $\Delta E^{\ddagger}_{strain}$ than **TS4** suggesting less geometry distortion as the electron-rich -CN group in **TS3** pivots towards the cationic pentanidium catalyst (Figure 4). For the XAT **TS2**, the stronger dipole interactions energy compensates the strain component resulting in negative $\Delta E^{\ddagger}_{activation}$ at -9.8 kcal/mol.

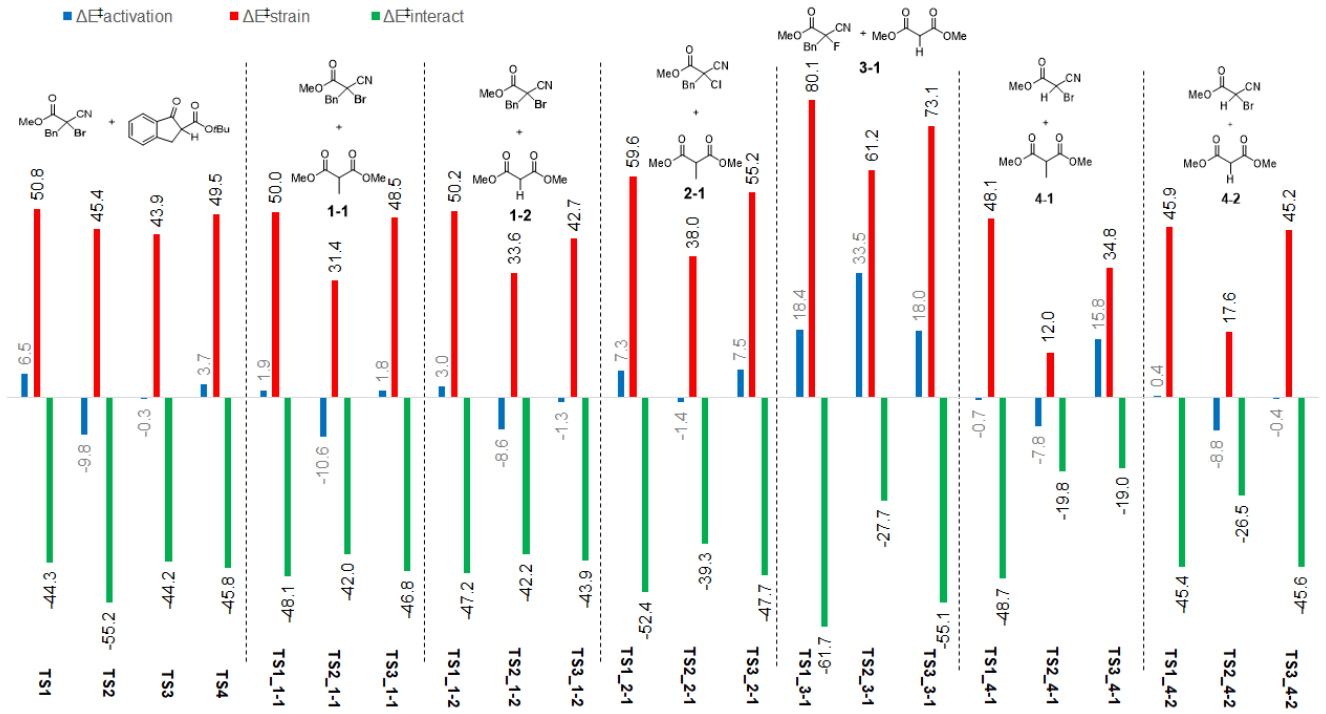

Figure 4 - Distortion/interaction activation strain model. DFT calculations at M11/def2-TZVP level of theory. Energy values are in kcal/mol.

The energies for the activation strain model, for the rest of the screened substrates in Table 1, are shown in Figure 4. Comparing the direct S_N2 energies for the bromides, ranked from highest to lowest (Table 1) - **TS1_1-2** ($\Delta G^{\ddagger}_{sol}$ = 26.2 kcal/mol), **TS1_1-1** (24.8 kcal/mol), **TS1_4-2** (18.6 kcal/mol) and **TS1_4-1** (17.6 kcal/mol) - the activation strain model $\Delta E^{\ddagger}_{activation}$ follows a similar trend (3.0, 1.9, 0.4 and -0.7 kcal.mol) with the direct S_N2 energy barriers becoming favourable as the bromide becomes unencumbered. As such, the direct S_N2 pathway becomes more accessible with the secondary halide, while quaternary-quaternary C-C bond formation favors the S_N2X manifold. It is also predicted that under higher reaction temperature, the direct S_N2 route could become thermodynamically competitive, despite the XAT step having a lower free energy barrier and a much higher second S_N2 free energy barrier for the less sterically impeded **4-1** and **4-2** (**TS3** free energy barrier of 24.2 and 20.0 kcal/mol relative to **INT6** + **BR2** respectively).

Across the halides (**1-1**, **2-1** and **3-1**), the S_N2 transition states - **TS1** and **TS3** - $\Delta E^{\ddagger}_{activation}$ and $\Delta E^{\ddagger}_{strain}$ increases with a significant jump for fluoride **3-1**. **TS1** and **TS3** $\Delta E^{\ddagger}_{strain}$ also increases from bromide to fluoride, which correlates to the higher energy cost required to break increasingly stronger C-X bonds, despite having a more negative $\Delta E^{\ddagger}_{interaction}$. The halide series also shows that the **TS1** $\Delta E^{\ddagger}_{activation}$ becomes more negative while **TS2** $\Delta E^{\ddagger}_{activation}$ becomes more positive, resulting in direct S_N2 becoming more competitive. Similarly, **TS2** $\Delta E^{\ddagger}_{strain}$ becomes more positive across the series which correlates to increase in their free energy barriers. It is also noteworthy that **TS2_2-1** has negative $\Delta E^{\ddagger}_{activation}$ of -1.4 kcal/mol, indicating that it is plausible for the chloride to undergo S_N2X. For fluoride **3-1**, a much higher $\Delta G^{\ddagger}_{sol}$ for **TS2** as compared to **TS1** could be correlated to the $\Delta E^{\ddagger}_{activation}$, that is -27.7 and -61.7 kcal/mol respectively, which could be attributed to a weaker σ*(C^{-}···F) interaction.

Activation strain energies for all computationally screened substrates in Table 1 and 2 are summarized in Table 3 and plotted in Figure 5. This allows appraisal of the free energy barriers with the activation strain model and predict if there are any important correlations relating to reactivity and the component $\Delta E^{\ddagger}_{activation}$, $\Delta E^{\ddagger}_{strain}$ and $\Delta E^{\ddagger}_{interaction}$. From Figure 5, the $\Delta E^{\ddagger}_{strain}$ for **TS1** averages 48 kcal/mol for Br, 65 kcal/mol for Cl and 80 kcal/mol for F, and $\Delta E^{\ddagger}_{interaction}$ averages -48 kcal/mol for Br, -53 kcal/mol for Cl and -62 kcal/mol for F. The trend for **TS2** is expected to be the same as **TS1**, with Br having the lowest barrier range (10 to 12 kcal/mol) and $\Delta E^{\ddagger}_{activation}$ within -10 to -9 kcal/mol. This is followed by Cl, where **TS2** free energy barrier range from 20 to 30 kcal/mol and $\Delta E^{\ddagger}_{activation}$ within -1 to 6 kcal/mol. Not surprisingly, F has the highest energy barrier and $\Delta E^{\ddagger}_{activation}$. The $\Delta E^{\ddagger}_{strain}$ for **TS2** averages 24 kcal/mol for Br, 45 kcal/mol for Cl and 61 kcal/mol for F and $\Delta E^{\ddagger}_{interaction}$ averages -33 kcal/mol for Br, -43 kcal/mol for Cl and -28 kcal/mol for F. For **TS3**, the barrier range for Br is 20 to 25 kcal/mol and $\Delta E^{\ddagger}_{activation}$ range from -1 to 2 kcal/mol; Cl has barrier of 24 to 43 kcal/mol and $\Delta E^{\ddagger}_{activation}$ from 5 to 19 kcal/mol; F has barrier of 39 kcal/mol and $\Delta E^{\ddagger}_{activation}$ of 19 kcal/mol. The $\Delta E^{\ddagger}_{strain}$ for **TS3** averages 47 kcal/mol for Br, 59 kcal/mol for Cl and 79 kcal/mol for F and $\Delta E^{\ddagger}_{interaction}$ averages -46 kcal/mol for Br, -49 kcal/mol for Cl and -61 kcal/mol for F. Analysis of Table 3 and Figure 4's activation barrier and activation strain model reveal strong correlation between the ease for X leaving group

and C-X bond strength (Br > Cl > F) to decreasing average **TS** free energy barrier and $\Delta E^{\ddagger}_{activation}$ in general (Br < Cl < F). Higher average $\Delta E^{\ddagger}_{strain}$ also resulted in higher **TS** barriers indicating that $\Delta E^{\ddagger}_{strain}$ and $\Delta E^{\ddagger}_{activation}$ are correlated. However, $\Delta E^{\ddagger}_{interaction}$ showed less impact on both barrier and $\Delta E^{\ddagger}_{activation}$ suggesting weak or no correlation.

Table 3 - Free energy barrier and distortion/interaction activation strain model comparison for all screened substrates. Calculated at M11/def2-TZVP/SMD(toluene)//M11/6-31G(d,p) and activation strain model at M11/def2-TZVP level of theory. Values are in kcal/mol.

Substrate set (#):	**1-1**	**1-2**	**4-1**	**4-2**	**3-1**	**2-1**	**2-2**	**2-3**	**2-4**	**2-5**	**2-6**	**2-7**
$\Delta G^{\ddagger}_{sol}$, TS1_#	24.8	26.2	17.6	18.6	38.4	28.6	30.1	27.5	38.1	33.9	36.8	33
$\Delta E^{\ddagger}_{activation}$	1.9	3.0	-0.7	-0.4	18.4	7.3	9.7	7.1	16.6	12.7	15.7	11.9
$\Delta E^{\ddagger}_{strain}$	50.0	50.2	48.1	45.2	80.1	59.6	57.5	57.1	71.7	70.0	71.1	69.6
$\Delta E^{\ddagger}_{interaction}$	-48.1	-47.1	-48.7	-45.6	-61.7	-52.4	-47.8	-50.0	-55.1	-57.3	-55.3	-57.7
$\Delta G^{\ddagger}_{sol}$, TS2_#	11.8	13.7	10.8	12.1	55.1	20.0	21.8	19.2	27.6	27.0	29.3	26.2
$\Delta E^{\ddagger}_{activation}$	-10.6	-8.6	-7.8	-8.8	33.5	-1.4	0.6	-2.6	5.1	2.9	5.9	2.4
$\Delta E^{\ddagger}_{strain}$	31.4	33.6	12.0	17.6	61.2	38.0	38.7	35.4	49.2	50.3	53.7	49.7
$\Delta E^{\ddagger}_{interaction}$	-42.0	-42.2	-19.8	-26.5	-27.7	-39.3	-38.0	-38.0	-44.1	-47.5	-47.8	-47.4
$\Delta G^{\ddagger}_{sol}$, TS3_#	23.3	19.7	24.2	20.0	38.6	27.7	24.1	24.4	42.9	31.8	32.0	31.4
$\Delta E^{\ddagger}_{activation}$	1.8	-1.3	2.3	0.4	18.6	7.5	4.8	5.1	18.6	11.2	8.9	10.5
$\Delta E^{\ddagger}_{strain}$	48.5	42.7	50.6	45.9	79.1	55.2	50.9	50.7	72.0	60.5	60.5	58.6
$\Delta E^{\ddagger}_{interaction}$	-46.8	-43.9	-48.3	-45.4	-60.5	-47.7	-46.1	-45.6	-53.5	-49.2	-51.6	-48.1

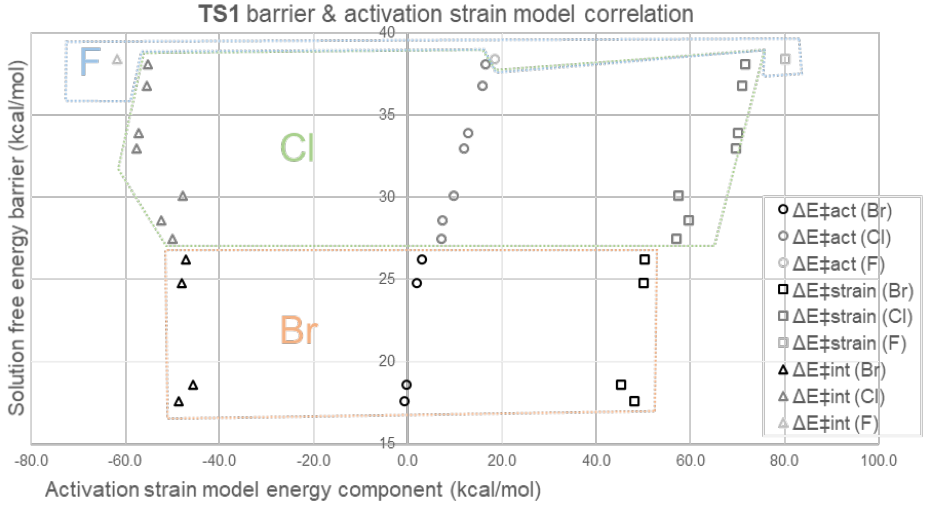

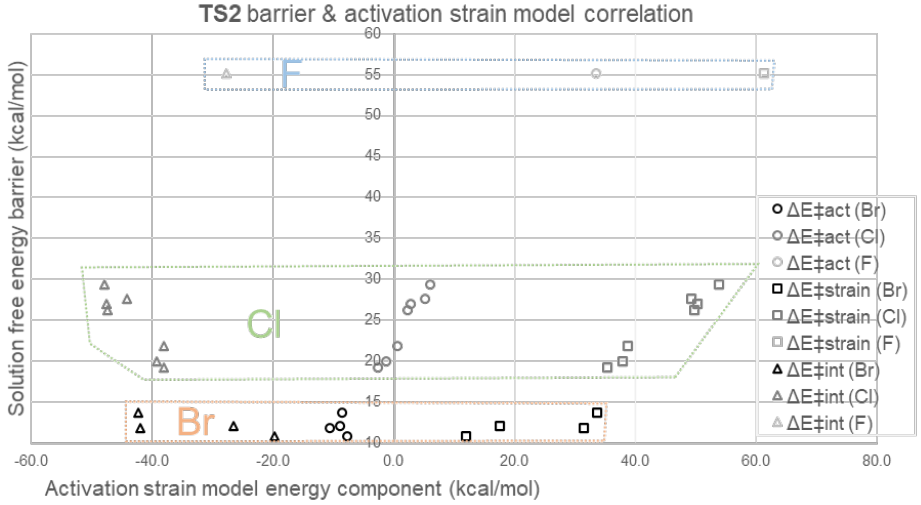

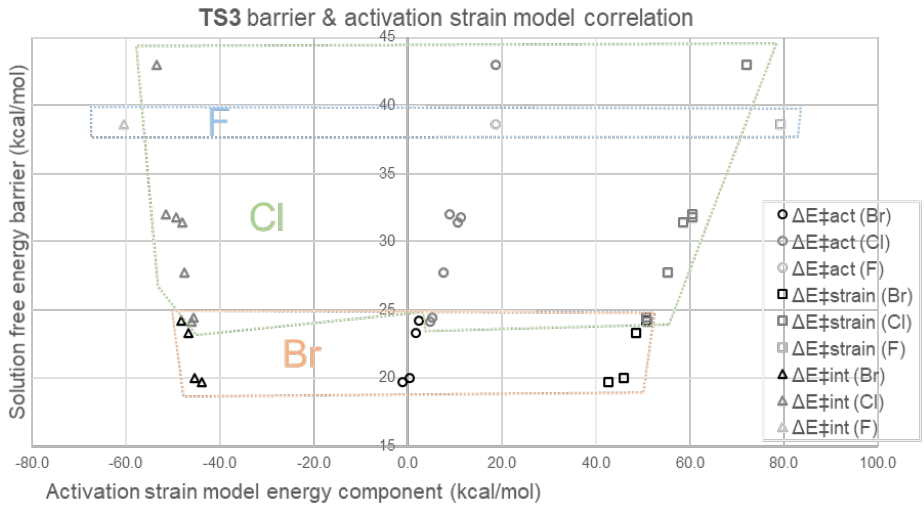

Figure 5 - Charts of TS barriers versus individual energy component of the activation strain model. Circle is $\Delta E^{\ddagger}_{activation}$, square is $\Delta E^{\ddagger}_{strain}$ and triangle $\Delta E^{\ddagger}_{interaction}$. Black color for bromide, gray for chloride and lighter gray for fluoride.

Full catalyst model (ONIOM). In order to probe the origin of stereochemistry in the asymmetric version of pentanidium catalyzed carbon-carbon bond formation, ONIOM calculations (see Computational Methods), at M11/def2-TZVP//M11/6-31G(d,p):PM6 level of theory, were performed for the full catalytic model. Despite the lowering of computational costs with ONIOM, such methods provide reasonable geometries and the DFT single-point calculations at M11/def2-TZVP level of theory will provide more accurate energies for the computational predictions.[10]

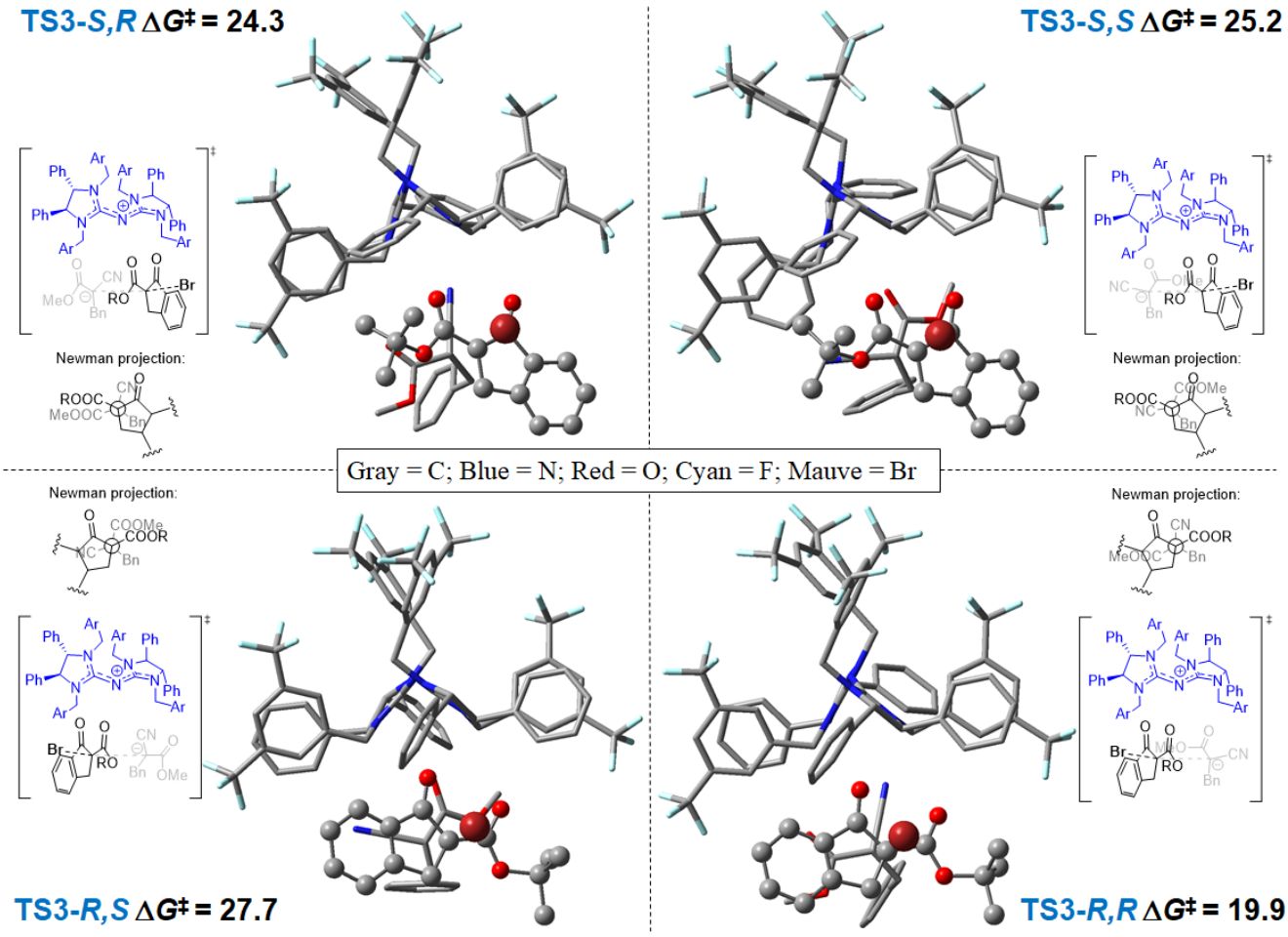

Figure 6 - Computational stereochemical prediction for C-C bond formation with full catalyst model. ONIOM M11/def2-TZVP//M11/6-31G(d,p):PM6 level of theory. Free energy values are in kcal/mol.

The truncated pentanidium DFT model suggests that the rate-determining and enantio-determining step as the second S_N2 substitution in the S_N2X manifold, after **INT6** and **BR2**. As such, the ONIOM model will focus on the **TS3** free energies for the four different stereochemical outcomes are shown in Figure 6, with the transition state **TS3-*R,R*** ($\Delta G^{\ddagger}$ = 19.9 kcal/mol) being the most stable, followed by **TS3-*S,R*** (24.3 kcal/mol), **TS3-*S,S*** (25.2 kcal/mol) and **TS3-*S,R*** (27.7 kcal/mol). More information about the pre-TS complexes can be found in the supporting information. The predicted stereochemistry of the major product corroborates the absolution configuration of the product, as determined by single-crystal X-ray diffraction data.

Further analysis of the transition state structures (Figure 6) revealed that the most optimal geometry of the nucleophile, when bound to the catalyst, occurs when the cyano group pivots towards the pentanidium moiety, generating the most stable transition state **TS3-*R,R*** and second most stable **TS3-*S,R***. In short, the pentanidium binds more favorably when the negatively charged cyano group is closer *via* electrostatic attraction in the ion-pair and predisposes the nucleophile in a *re* orientation. This stereochemical preference is further distinguished between **TS3-*R,R*** and **TS3-*S,R*** when the cyclic ketoester halide approaches towards the *re*-oriented nucleophile, with the benzyl in a preferentially unhindered position, affording the experimentally obtained *R,R* product. As the barrier through ***TS3-R,R*** is most kinetically accessible, it is predicted that the quick consumption of the *S*-configuration **BR2** will drive the isomerization process from *R*-**BR2** to *S*-**BR2**.

■ CONCLUSION

In conclusion, the DFT model suggests that the reaction mechanism for the pentanidium catalyzed construction of sterically congested vicinal quaternary $C(sp^3)$-$C(sp^3)$ bond proceeds *via* a halogenophilic S_N2X manifold. In a bid to rationalize the mechanistic dichotomy between direct S_N2 or S_N2X process, computational screening of cyanoester and malonates with their derivatives of varying steric bulkiness showed that the direct S_N2 could be favored if the cyanoester bromide was less sterically demanding. Generally, the calculations predict that the S_N2X manifold's **TS2** (XAT) activation free energy barriers are more accessible and lower for the bromides and chlorides than **TS1** (S_N2), and the thermodynamic stability of the intermediates **INT6** and **BR2** or **Cl2** in the presence of base allow the dynamic interconversion of the halides to be feasible. This in turn affords the high enantioselectivity through dynamic kinetic resolution concordant with previous reports.

These theoretical calculations thus corroborate to the observed experimental data which represents a successful example of a S_N2X substitution reaction in assembling highly desirable yet synthetically challenging congested $C(sp^3)$-$C(sp^3)$ bond and offer guidance to predicting the optimal choice of reaction conditions or substrates. The plausible scope of bromides is further extended as computationally screening of various halides also helped predict the suitability of chlorides for the S_N2X which the experimental work is currently ongoing. Whilst the computational data presented here only described a single reaction system, the mechanistic insights into the halogenophilic S_N2X manifold can be used as platform to develop reaction design strategies to afford other synthetically challenging molecules. To this end, further experimental and computational studies on harnessing and discovering other S_N2X reactivities are currently underway.

ASSOCIATED CONTENT

Supporting Information

Computational supporting information and material is available free of charge via the internet at http://pubs.acs.org.

AUTHOR INFORMATION

Corresponding Author

richmond_lee@uow.edu.au

Notes

The authors declare no competing financial interest.

ACKNOWLEDGMENT

We gratefully acknowledge financial support from the Australian Research Council (DE210100053, RL), UOW RITA Grant 2021 (HY and RL) and a UOW Vice Chancellor's Research Fellowship (RL). We would also like to acknowledge Nanyang Technological University for Tier 1 grants (RG1/19 and RG2/20) and Ministry of Education (Singapore) Tier 2 grants (MOE2019-T2-1-091, CHT). Computational resources are provided by the National Computing Infrastructure (Australia) through the Merit Allocation (NCMAS) and UOW Partnership Schemes. We would like to thank Dr. Davin Tan for helpful discussions.

REFERENCES

(1) Adero, P. O.; Amarasekara, H.; Wen, P.; Bohé, L.; Crich, D. The Experimental Evidence in Support of Glycosylation Mechanisms at the S $_N$ 1–S $_N$ 2 Interface. *Chem. Rev.* **2018**, *118* (17), 8242–8284. https://doi.org/10.1021/acs.chemrev.8b00083.

(2) HUGHES, E. D.; INGOLD, C. K.; WHITFIELD, I. C. The Walden Inversion in the Replacement of Hydroxyl by Halogen. *Nature* **1941**, *147* (3720), 206–207. https://doi.org/10.1038/147206c0.

(3) Otto, R.; Brox, J.; Trippel, S.; Stei, M.; Best, T.; Wester, R. Single Solvent Molecules Can Affect the Dynamics of Substitution Reactions. *Nat. Chem.* **2012**, *4* (7), 534–538. https://doi.org/10.1038/nchem.1362.

(4) Stei, M.; Carrascosa, E.; Kainz, M. A.; Kelkar, A. H.; Meyer, J.; Szabó, I.; Czakó, G.; Wester, R. Influence of the Leaving Group on the Dynamics of a Gas-Phase SN2 Reaction. *Nat. Chem.* **2016**, *8* (2), 151–156. https://doi.org/10.1038/nchem.2400.

(5) Sutar, R. L.; Huber, S. M. Catalysis of Organic Reactions through Halogen Bonding. *ACS Catal.* **2019**, *9* (10), 9622–9639. https://doi.org/10.1021/acscatal.9b02894.

(6) Zefirov, N. S.; Makhon'kov, D. I. X-Philic Reactions. *Chem. Rev.* **1982**, *82* (6), 615–624. https://doi.org/10.1021/cr00052a004.

(7) Bento, A. P.; Bickelhaupt, F. M. Nucleophilicity and Leaving-Group Ability in Frontside and Backside S $_N$ 2 Reactions. *J. Org. Chem.* **2008**, *73* (18), 7290–7299. https://doi.org/10.1021/jo801215z.

(8) Fu, Y.; Bernasconi, L.; Liu, P. Ab Initio Molecular Dynamics Simulations of the S $_N$ 1/S $_N$ 2 Mechanistic Continuum in Glycosylation Reactions. *J. Am. Chem. Soc.* **2021**, *143* (3), 1577–1589. https://doi.org/10.1021/jacs.0c12096.

(9) Zhang, X.; Ren, J.; Tan, S. M.; Tan, D.; Lee, R.; Tan, C.-H. An Enantioconvergent Halogenophilic Nucleophilic Substitution (S $_N$ 2X) Reaction. *Science* **2019**, *363* (6425), 400–404. https://doi.org/10.1126/science.aau7797.

(10) Ren, J.; Ban, X.; Zhang, X.; Tan, S. M.; Lee, R.; Tan, C.-H. Kinetic and Dynamic Kinetic Resolution of Racemic Tertiary Bromides by Pentanidium-Catalyzed Phase-Transfer Azidation. *Angew. Chem. - Int. Ed.* **2020**, *59* (23), 9055–9058. https://doi.org/10.1002/anie.202000138.

(11) Ban, X.; Fan, Y.; Kha, T.-K.; Lee, R.; Kee, C. W.; Jiang, Z.; Tan, C.-H. Pentanidium-Catalyzed Direct Assembly of Vicinal All-Carbon Quaternary Stereocenters through C(Sp ^{3})-C(Sp ^{3}) Bond Formation. *CCS Chem.* **2021**, 1–21. https://doi.org/10.31635/ccschem.021.202101013.

(12) Zhang, X.; Tan, C.-H. Stereospecific and Stereoconvergent Nucleophilic Substitution Reactions at Tertiary Carbon Centers. *Chem* **2021**, *7* (6), 1451–1486. https://doi.org/10.1016/j.chempr.2020.11.022.

(13) Pracht, P.; Bohle, F.; Grimme, S. Automated Exploration of the Low-Energy Chemical Space with Fast Quantum Chemical Methods. *Phys. Chem. Chem. Phys.* **2020**, *22* (14), 7169–7192. https://doi.org/10.1039/C9CP06869D.

(14) Bannwarth, C.; Ehlert, S.; Grimme, S. GFN2-XTB—An Accurate and Broadly Parametrized Self-Consistent Tight-Binding Quantum Chemical Method with Multipole Electrostatics and Density-Dependent Dispersion Contributions. *J. Chem. Theory Comput.* **2019**, *15* (3), 1652–1671. https://doi.org/10.1021/acs.jctc.8b01176.

(15) Frisch, M. J.; Trucks, G. W.; Schlegel, H. B.; Scuseria, G. E.; Robb, M. A.; Cheeseman, J. R.; Scalmani, G.; Barone, V.; Petersson, G. A.; Nakatsuji, H.; Li, X.; Caricato, M.; Marenich, A. V.; Bloino, J.; Janesko, B. G.; Gomperts, R.; Mennucci, B.; Hratchian, H. P.; Ortiz, J. V.; Izmaylov, A. F.; Sonnenberg, J. L.; Williams-Young, D.; Ding, F.; Lipparini, F.; Egidi, F.; Goings, J.; Peng, B.; Petrone, A.; Henderson, T.; Ranasinghe, D.; Zakrzewski, V. G.; Gao, J.; Rega, N.; Zheng, G.; Liang, W.; Hada, M.; Ehara, M.; Toyota, K.; Fukuda, R.; Hasegawa, J.; Ishida, M.; Nakajima, T.; Honda, Y.; Kitao, O.; Nakai, H.; Vreven, T.; Throssell, K.; Montgomery, J. A., Jr.; Peralta, J. E.; Ogliaro, F.; Bearpark, M. J.; Heyd, J. J.; Brothers, E. N.; Kudin, K. N.; Staroverov, V. N.; Keith, T. A.; Kobayashi, R.; Normand, J.; Raghavachari, K.; Rendell, A. P.; Burant, J. C.; Iyengar, S. S.; Tomasi, J.; Cossi, M.; Millam, J. M.; Klene, M.; Adamo, C.; Cammi, R.; Ochterski, J. W.; Martin, R. L.; Morokuma, K.; Farkas, O.; Foresman, J. B.; Fox, D. J. *Gaussian˜16 Revision A.03*; 2016.

(16) Peverati, R.; Truhlar, D. G. Improving the Accuracy of Hybrid Meta-GGA Density Functionals by Range Separation. *J. Phys. Chem. Lett.* **2011**, *2* (21), 2810–2817. https://doi.org/10.1021/jz201170d.

(17) Ditchfield, R.; Hehre, W. J.; Pople, J. A. Self-Consistent Molecular-Orbital Methods. IX. An Extended Gaussian-Type Basis for Molecular-Orbital Studies of Organic Molecules. *J. Chem. Phys.* **1971**, *54* (2), 724–728. https://doi.org/10.1063/1.1674902.

(18) Bergner, A.; Dolg, M.; Küchle, W.; Stoll, H.; Preuß, H. *Ab Initio* Energy-Adjusted Pseudopotentials for Elements of Groups 13–17. *Mol. Phys.* **1993**, *80* (6), 1431–1441. https://doi.org/10.1080/00268979300103121.

(19) Dolg, M.; Wedig, U.; Stoll, H.; Preuss, H. Energy-adjusted *a b i n i t i o* Pseudopotentials for the First Row Transition Elements. *J. Chem. Phys.* **1987**, *86* (2), 866–872. https://doi.org/10.1063/1.452288.

(20) Ribeiro, R. F.; Marenich, A. V.; Cramer, C. J.; Truhlar, D. G. Use of Solution-Phase Vibrational Frequencies in Continuum Models for the Free Energy of Solvation. *J. Phys. Chem. B* **2011**, *115* (49), 14556–14562. https://doi.org/10.1021/jp205508z.

(21) Marenich, A. V.; Cramer, C. J.; Truhlar, D. G. Universal Solvation Model Based on Solute Electron Density and on a Continuum Model of the Solvent Defined by the Bulk Dielectric Constant and Atomic Surface Tensions. *J. Phys. Chem. B* **2009**, *113* (18), 6378–6396. https://doi.org/10.1021/jp810292n.

(22) Weigend, F. Accurate Coulomb-Fitting Basis Sets for H to Rn. *Phys. Chem. Chem. Phys.* **2006**, *8* (9), 1057. https://doi.org/10.1039/b515623h.

(23) Weigend, F.; Ahlrichs, R. Balanced Basis Sets of Split Valence, Triple Zeta Valence and Quadruple Zeta Valence Quality for H to Rn: Design and Assessment of Accuracy. *Phys. Chem. Chem. Phys.* **2005**, *7* (18), 3297. https://doi.org/10.1039/b508541a.

(24) Ho, J.; Klamt, A.; Coote, M. L. Comment on the Correct Use of Continuum Solvent Models. *J. Phys. Chem. A* **2010**, *114* (51), 13442–13444. https://doi.org/10.1021/jp107136j.

(25) Levandowski, B. J.; Hamlin, T. A.; Bickelhaupt, F. M.; Houk, K. N. Role of Orbital Interactions and Activation Strain (Distortion Energies) on Reactivities in the Normal and Inverse Electron-Demand Cycloadditions of Strained and Unstrained Cycloalkenes. *J. Org. Chem.* **2017**, *82* (16), 8668–8675. https://doi.org/10.1021/acs.joc.7b01673.

(26) Bickelhaupt, F. M.; Houk, K. N. Analyzing Reaction Rates with the Distortion/Interaction-Activation Strain Model. *Angew. Chem. Int. Ed.* **2017**, *56* (34), 10070–10086. https://doi.org/10.1002/anie.201701486.
(27) Wolters, L. P.; Bickelhaupt, F. M. The Activation Strain Model and Molecular Orbital Theory: Activation Strain Model and Molecular Orbital Theory. *Wiley Interdiscip. Rev. Comput. Mol. Sci.* **2015**, *5* (4), 324–343. https://doi.org/10.1002/wcms.1221.
(28) van Zeist, W.-J.; Bickelhaupt, F. M. The Activation Strain Model of Chemical Reactivity. *Org. Biomol. Chem.* **2010**, *8* (14), 3118. https://doi.org/10.1039/b926828f.
(29) Legault, C. Y.; Garcia, Y.; Merlic, C. A.; Houk, K. N. Origin of Regioselectivity in Palladium-Catalyzed Cross-Coupling Reactions of Polyhalogenated Heterocycles. *J. Am. Chem. Soc.* **2007**, *129* (42), 12664–12665. https://doi.org/10.1021/ja075785o.
(30) Bickelhaupt, F. M. Understanding Reactivity with Kohn-Sham Molecular Orbital Theory: E2-SN2 Mechanistic Spectrum and Other Concepts. *J. Comput. Chem.* **1999**, *20* (1), 114–128. https://doi.org/10.1002/(SICI)1096-987X(19990115)20:1<114::AID-JCC12>3.0.CO;2-L.
(31) Vreven, T.; Morokuma, K.; Farkas, Ö.; Schlegel, H. B.; Frisch, M. J. Geometry Optimization with QM/MM, ONIOM, and Other Combined Methods. I. Microiterations and Constraints. *J. Comput. Chem.* **2003**, *24* (6), 760–769. https://doi.org/10.1002/jcc.10156.
(32) Stewart, J. J. P. Optimization of Parameters for Semiempirical Methods V: Modification of NDDO Approximations and Application to 70 Elements. *J. Mol. Model.* **2007**, *13* (12), 1173–1213. https://doi.org/10.1007/s00894-007-0233-4.
(33) Yang, H.; Wong, M. W. Application of Halogen Bonding to Organocatalysis: A Theoretical Perspective. *Molecules* **2020**, *25* (5), 1045. https://doi.org/10.3390/molecules25051045.
(34) Cavallo, G.; Metrangolo, P.; Milani, R.; Pilati, T.; Priimagi, A.; Resnati, G.; Terraneo, G. The Halogen Bond. *Chem. Rev.* **2016**, *116* (4), 2478–2601. https://doi.org/10.1021/acs.chemrev.5b00484.
(35) Falivene, L.; Cao, Z.; Petta, A.; Serra, L.; Poater, A.; Oliva, R.; Scarano, V.; Cavallo, L. Towards the Online Computer-Aided Design of Catalytic Pockets. *Nat. Chem.* **2019**, *11* (10), 872–879. https://doi.org/10.1038/s41557-019-0319-5.